


## Article

# Experimental Study on Mechanical Properties and Stability Analysis of Structural Plane under Unloading Normal Stress

Feng Jiao, Jiang Xu, Shoujian Peng <sup>\*</sup>, Meixin He and Xinrui Zhang

State Key Laboratory of Coal Mine Disaster Dynamics and Control, Chongqing University, Chongqing 400040, China

\* Correspondence: sjpeng@cqu.edu.cn; Tel.: +86-186-808-71822

**Abstract:** Excavation in rock induces the unloading of stress in excavation-disturbed zones and can cause the structural plane to reach shear failure due to the unloading of normal stress. Unloading normal stress tests of a regular sawtooth structural plane were conducted in this study to investigate the influence of the unloading velocities ( $v$ ) and asperity angles ( $\theta$ ) on mechanical properties and the stability of the structural plane. The average value of normal displacement ( $D_{u1}$ ) and the shear displacement of unloading ( $D_{su}$ ) gradually increases with an increase in  $\theta$  and  $D_{u1}$  accounts for 59.70%, 31.81%, and 18.60% of the height of a single asperity under different  $\theta$ . However,  $D_{u2}$ ,  $D_s$ , and the unloading capacity ( $\Delta\sigma_n$ ) gradually decreased. Moreover,  $D_s$  account for 24.52%, 11.61%, and 7.4% of the length of a single asperity, respectively. With an increase in  $\theta$  and  $v$ , three-dimensional (3D) morphology parameters and normal deformation energy ( $U_n$ ) decreased gradually, indicating that the damage degree of the structural plane increases. The analysis of the evolution of the gap width of the structural plane at the initial point, unloading point, and instability point indicates that the greater the  $\theta$  or the smaller the  $v$ , the lower would be the likelihood for the structural plane to be damaged. Concurrently, its instability is more sudden and the impact tendency is stronger.

**Keywords:** unloading normal stress; asperity angles; unloading velocities; energy evolution; 3D morphology parameters; gap width



**Citation:** Jiao, F.; Xu, J.; Peng, S.; He, M.; Zhang, X. Experimental Study on Mechanical Properties and Stability Analysis of Structural Plane under Unloading Normal Stress. *Sustainability* **2022**, *14*, 15656. <https://doi.org/10.3390/su142315656>

Academic Editor: Wen Cheng Liu

Received: 10 October 2022

Accepted: 13 November 2022

Published: 24 November 2022

**Publisher's Note:** MDPI stays neutral with regard to jurisdictional claims in published maps and institutional affiliations.



**Copyright:** © 2022 by the authors. Licensee MDPI, Basel, Switzerland. This article is an open access article distributed under the terms and conditions of the Creative Commons Attribution (CC BY) license (<https://creativecommons.org/licenses/by/4.0/>).

## 1. Introduction

Excavation causes stress redistribution, which typically leads to the unloading of stress in the excavation-disturbed area and results in engineering disasters, such as rock bursts, thereby resulting in substantial casualties and economic losses [1–3]. Since the founding of New China more than 60 years ago and the continuous development of resources, shallow energy resources have been gradually exhausted. Thus, the demand for deep resources is increasing. However, as the depth increases, the frequency and scale of rock bursts gradually increase [4–6]. Therefore, it is particularly critical to study the instability and failure mechanism of structural planes under unloading conditions.

Numerous confining pressure relief tests have been conducted under the condition of a triaxial test and promising results have been obtained [7–9]. The results show that specimen failure is primarily influenced by the loading path and unloading velocity [10–16]. The rock samples exhibit completely different mechanical properties during loading and unloading [17]. During unloading instability and failure, the degree of damage is closely related to the unloading velocity [18]; the tensile cracks and degree of failure of rock samples increase with an increase in the unloading velocity [19]. Moreover, the failure strength of rock under unloading conditions is lower than that under loading conditions [20]. Granite is more prone to failure at a medium unloading velocity than at high or low unloading velocities [21,22]. With an increase in the unloading velocity, the degree of rock failure increases gradually, owing to an increase in the strain energy release capacity [23,24], and the volume expansion becomes more significant [25]. Under the condition of triaxial unloading,

the failure mode of the specimen becomes more complex than that of the conventional triaxial test [26,27], and the failure strain at unloading is less than that at loading [28]. Under the condition of an unloading test, the initial confining pressure is also the main factor affecting the mechanical properties of rock. During loading, the rock samples exhibit clear brittle ductile transition characteristics as the confining pressure increases [29]. An increase in the confining pressure limits the radial deformation of rock samples [30]; therefore, more cracks are produced before failure [31,32]. Moreover, the brittle failure characteristics of rock samples become more apparent as the confining pressure increases [33–35]. The failure characteristics of rock samples can be determined by the energy evolution law during loading and unloading [36,37]. The evolution of energy is closely related to the fracture initiation, development, and final failure of rock samples and it controls the failure mode of rock samples [38,39]. Moreover, acoustic emission signal conclusion in the test process can be used for verification [40].

However, the triaxial unloading test cannot directly and effectively model the shear failure mechanism of rock that has suffered only from unloading normal stress [41]. Owing to geological processes, there are several structural planes in rock mass. Therefore, by considering the regular sawtooth structural plane as the object, this study adopted the unloading normal stress test under the action of compression and shear load to explore the influence mechanism of the unloading velocity and asperity angle on the deformation and strength of the structural plane and the law of energy evolution. The results provide a reference for the instability and failure of engineering fractured rock mass as well as disaster prevention.

## 2. Test Method

### 2.1. Specimen Preparation

The surface of a natural rock structure has irregular three-dimensional morphology and its measurement incurs the disadvantage of artificial subjectivity [42,43]. Moreover, the structural plane is damaged after a test and cannot be reused. Therefore, this method used regular sawtooth structural planes poured with cement mortar as the test objects. Most existing structural plane pouring molds can only be formed individually [44]; the mechanical properties of the structural plane are affected by the pouring batch, mixing uniformity and curing time. Only the mold of the upper structural plane is taken as an example, as shown in Figure 1. The mold primarily comprises a concave—convex base, long and short diaphragms, and clamping and fixing devices. A total of 10 structural planes with asperity angles of  $\theta = 15^\circ$ ,  $30^\circ$ , and  $45^\circ$  can be formed simultaneously with corresponding single asperity heights of 0.67 mm, 1.44 mm, and 2.5 mm; the length of the bottom edge is 5 mm.

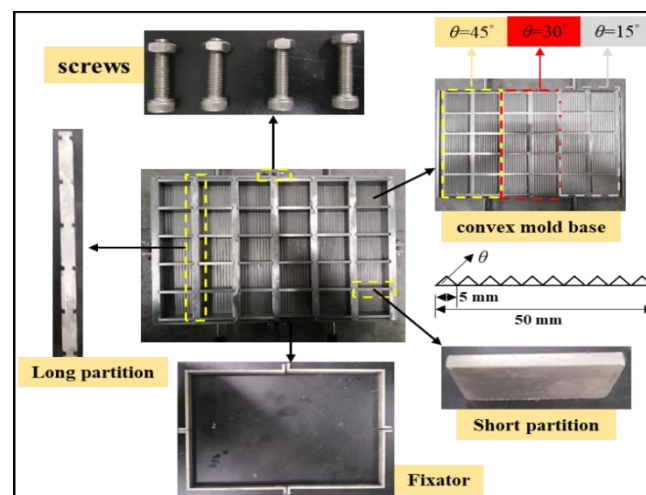
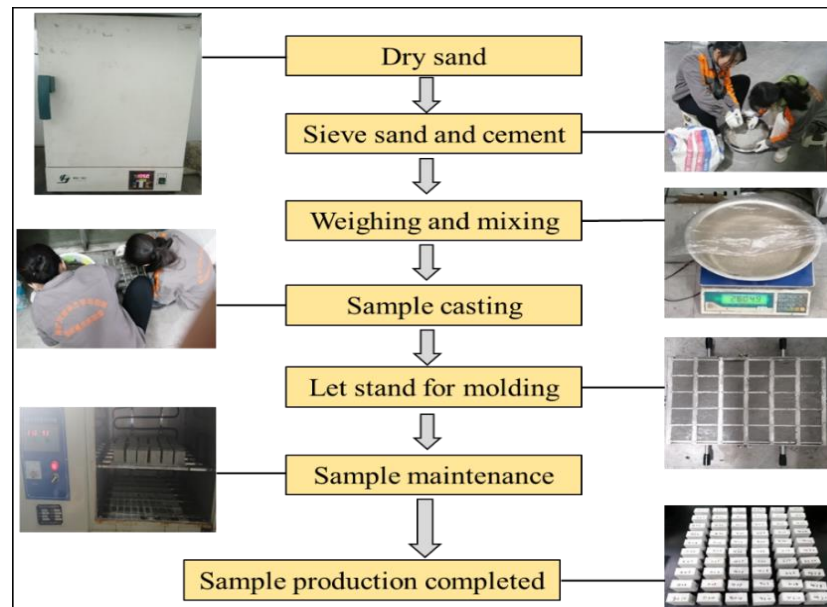


Figure 1. Manufacturing mold of regular sawtooth structural plane.

The steps to manufacture a regular sawtooth structural plane are as follows:

- ◆ The sand is dried in an oven at 105 °C for 24 h and then screened with a 120-mesh screen to ensure the uniformity of the sand particles. Cement with a strength of 32.5 R is also screened to ensure the uniformity of the material particles.
- ◆ Cement, sand, and water are evenly mixed according to the proportions of 3:2:1.5. Subsequently, tap water is added, and the materials are fully mixed. The mixture is then placed on a shaking table and the vibration drives out any bubbles.
- ◆ The evenly stirred materials are poured into the mold while being stirred with a vibrating rod to further discharge the bubbles.
- ◆ After pouring, the mixture is left to stand at a temperature of 20 °C for 3 d. The structural plane is demolded after complete solidification and cured for 28 d. The manufacturing process of the structural plane is shown in Figure 2. Additionally, mechanical parameters are shown in Table 1. According to Table 1, there are nine test conditions in total, in which each test condition is repeated three times, and 27 samples are required.



**Figure 2.** Manufacturing process of structural plane.

**Table 1.** Mechanical parameters of cement mortar.

$\sigma_n$ /MPa	$\mu$	$E$ /GPa	$c$ /MPa	$\varphi_b$ /°
15	0.27	3.39	2.84	28

where  $\sigma_n$  is the uniaxial compressive strength;  $\mu$  is Poisson's ratio;  $E$  is elastic modulus,  $c$  is cohesion; and  $\varphi_b$  is the internal friction angle.

The test is conducted on the self-developed “coal rock shear–seepage coupling” test system [45]. The system is primarily composed of a servo control loading system, fluid source loading system, shear box and sealing system, and control and data acquisition system. It can be used to conduct coal and rock shear tests under different loading modes (constant normal stress, constant normal displacement, and constant normal stiffness). The maximum test force in both the axial and shear directions is 300 kN and the displacement rate control range is 0–100 mm/min, as shown in Figure 3a. Before and after shearing, an OKIO-B non-contact optical 3D scanner is used to scan the structural plane, as shown in Figure 3b.

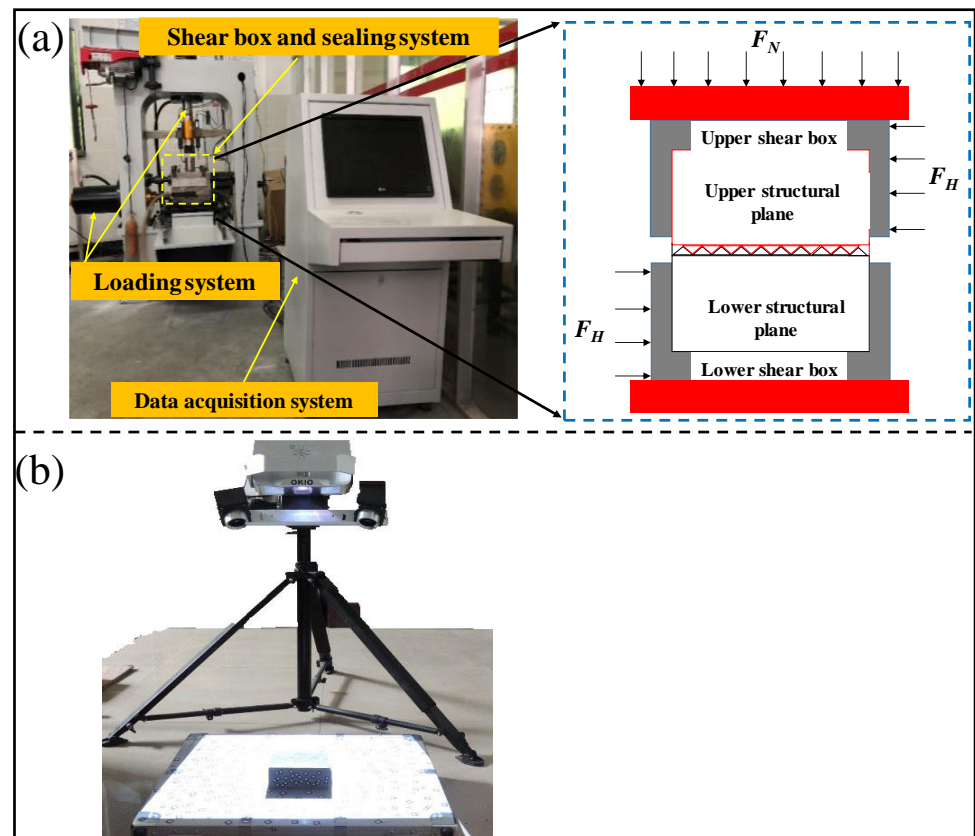


**Figure 3.** Schematic of test system (a) coal rock shear–seepage coupling test system; (b) 3D morphology scanner of structural plane.

## 2.2. Experimental Scheme

The steps followed for the unloading normal stress test are as follows:

First step: Normal stress at a set value of  $\sigma_{n0}$  is applied. The force loading mode is adopted, and the rate of loading is 0.1 kN/s.

Second step: The value of  $\sigma_{n0}$  is unchanged and the shear stress is then applied to a target value of  $\tau_0$ . The force control mode is also adopted for loading and the rate of loading is 0.02 kN/s.

Third step: The value of  $\tau_0$  remains unchanged and the normal stress is unloaded until the structural plane experiences instability failure. The force control mode is adopted and the unloading velocities ( $v$ ) are 0.05 kN/s, 0.1 kN/s, and 0.15 kN/s.

The following parameters are chosen as an example to illustrate the test steps, as shown in Figure 4 ( $\sigma_{n0} = 2.25$  MPa,  $\theta = 15^\circ$ ,  $v = 0.1$  kN/s and  $\tau_0 = 5.384$  MPa).

The general principle of setting test parameters is as follows: (1) It is important to ensure that the structural plane will not be damaged before  $\tau_0$  is applied; therefore,  $\sigma_{n0}$  is less than the uniaxial compressive strength ( $\sigma_n$ ) of the structural plane. (2) To determine the selection range of  $\tau_0$  under different  $\sigma_{n0}$ , it is necessary to conduct a direct shear test on the structural plane. The value of  $\tau_0$  is between 0 MPa and the peak shear strength under the corresponding normal stress. Within this range, the specimen would not experience macro shear failure before the unloading normal stress and it would be damaged when the unloading  $\sigma_{n0}$  goes to zero. Using the uniaxial test on similar materials,  $\sigma_n = 15$  MPa is obtained. According to the general principle,  $\sigma_{n0} = 15\%\sigma_n$ . Based on the peak shear strength obtained from the direct shear test under CNL conditions,  $\tau_0$  is set as 5.384 MPa. The test scheme is shown in Table 2.

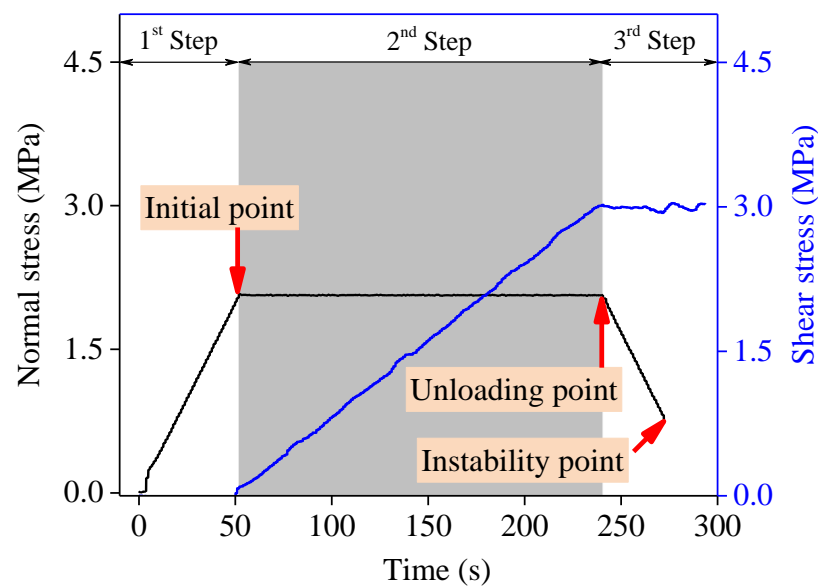


Figure 4. Test steps.

Table 2. Test scheme.

$\theta$ (°)	$\sigma_{n0}$ (MPa)	$\tau_0$ (MPa)	$v$ (kN/s)
15	2.25	5.384	0.05
			0.10
			0.15
30	2.25	5.384	0.05
			0.10
			0.15
45	2.25	5.384	0.05
			0.10
			0.15

### 3. Test Results and Analysis

#### 3.1. Deformation

##### 3.1.1. Displacement Histories

The displacement vs. time curves are shown in Figure 5.

In the first step, when the applied normal stress reaches  $\sigma_{n0}$ , the uniaxial test on the rock shows that the axial stress and axial displacement have a nonlinear relationship. Similarly, from the normal loading and unloading tests of the structural plane, it can also be observed that the normal stress and normal displacement are nonlinear in the loading stage. Therefore, the normal displacement increases nonlinearly and the rate of increase decreases gradually.

In the second step, the structural plane is subjected to both normal and shear stresses. Therefore, when applying the shear load, the shear displacement increases linearly with an increase rate of 0.001 mm/s. Meanwhile, the normal displacement increases slightly and the increase is between 0–0.098 mm. The direct shear test results of the structural plane indicate that the structural plane is compressed first. In other words, when the shear stress is applied to the structural plane to overcome the evident sliding of static friction, the crack between the upper and lower structural planes is gradually compressed.

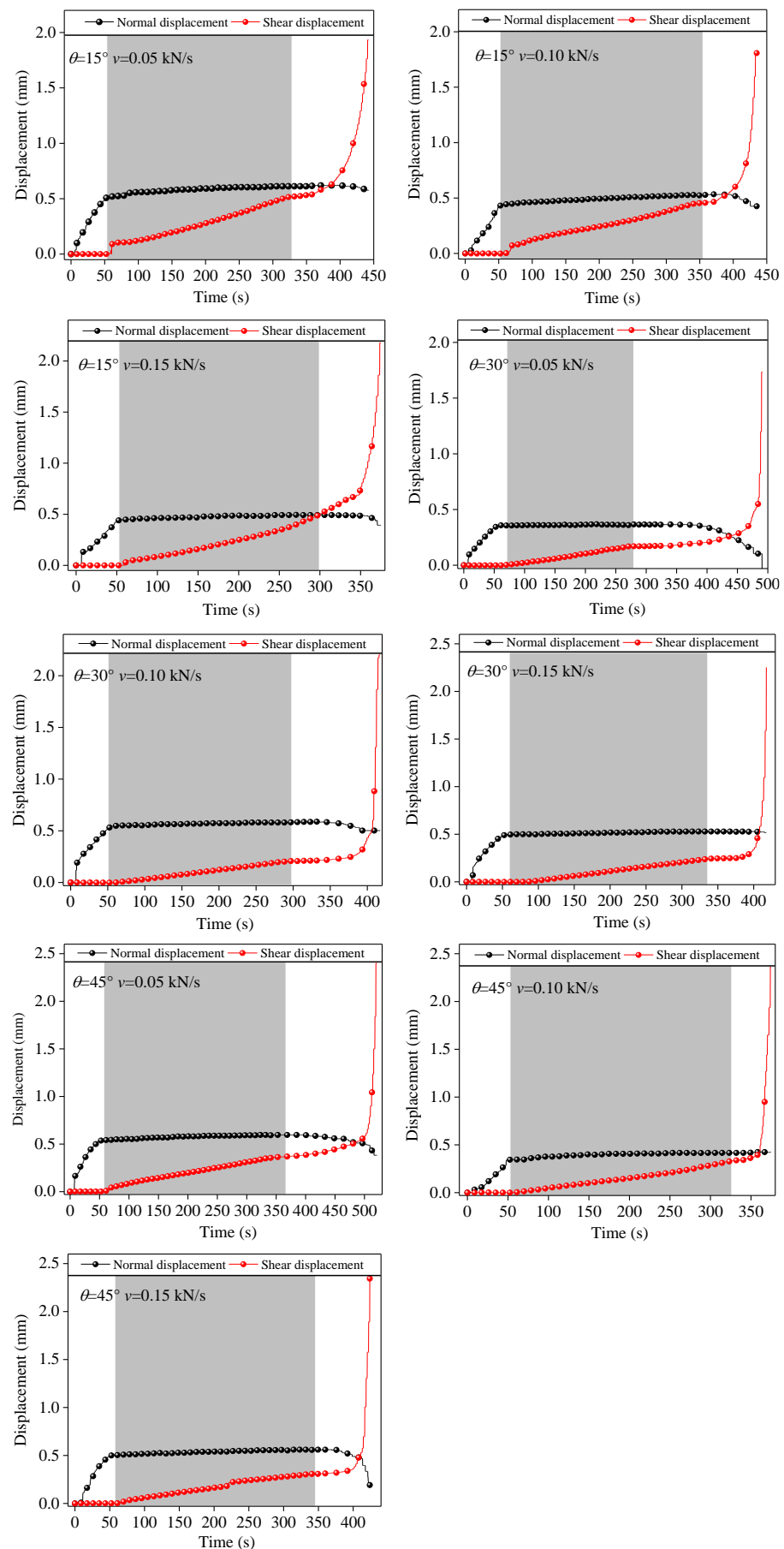
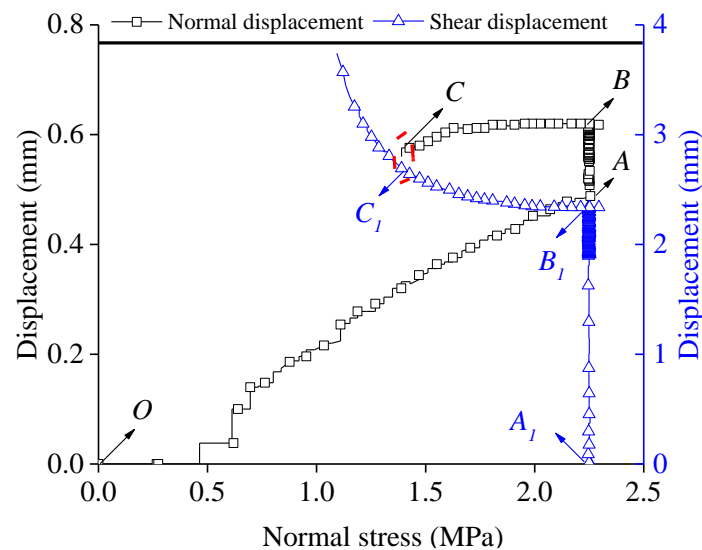


Figure 5. Shear and normal displacements vs. time curves.

In the third step, with a decrease in the normal stress, the normal displacement decreases nonlinearly and the reduction rate increases gradually. However, the shear displacement increases nonlinearly until the structural plane produces instability and slip and the rate increases gradually. This occurs because from the beginning of unloading to the instability of the structural plane, the normal elastic deformation energy is released owing to the reduction in normal stress. The structural plane rises along the asperities, resulting in shear expansion. The two stresses combine to gradually reduce the normal displacement of the structural plane. As the normal stress decreases, the static friction between the structural planes gradually decreases; thus, the structural plane moves forward and the corresponding shear displacement increases. When the normal stress is reduced to the critical point of instability, with a continuous reduction in the normal stress, there is clear shear slip on the structural plane. If the structural plane is slip damaged, the shear displacement increases rapidly in a very short time.

### 3.1.2. Characteristic Displacement

Using the values  $\theta = 15^\circ$  and  $v = 0.05$  kN/s as an example, the displacement—normal stress curve is shown in Figure 6.



**Figure 6.** Shear and normal displacements vs. normal stress curve.

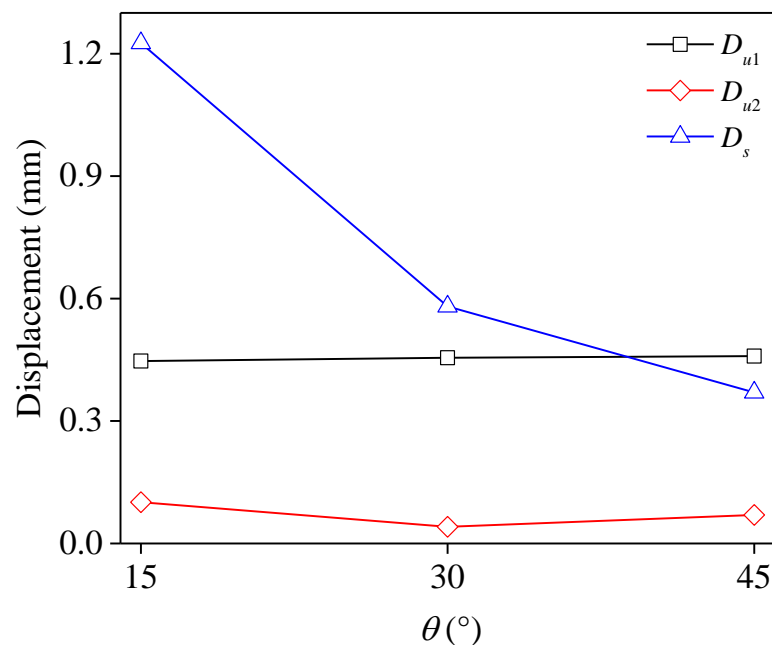
In Figure 6,  $O$  is the starting point of the experiment and the same numbered points (such as  $A$  and  $A_1$ ) represent the normal displacement and shear displacement at the same time point.  $A$  is the normal loading completion point,  $B$  is the unloading normal stress point, and  $C$  is the normal displacement value corresponding to the normal unloading instability. The corresponding  $A_1$ ,  $B_1$ , and  $C_1$  are three stages corresponding to the shear displacement. The characteristic points are labeled on the curve and the characteristic displacement is defined according to the characteristic points. The displacement is defined under loading normal stress  $D_{u1}$  (average value of normal displacement of  $OA$ ). While applying shear stress to  $\tau_0$ , the change in normal displacement is  $D_{u2}$  (the average value of the displacement difference between points  $B$  and  $A$ ). We define the variation in shear displacement (the average difference between the displacement of points  $B_1$  and  $A_1$ ), the shear displacement of unloading  $D_{su}$  (difference between displacements at points  $C_1$  and  $B_1$ ), and the normal displacement of unloading  $D_{nu}$  (displacement difference between points  $B$  and  $C$ ). The normal stress at failure is  $\sigma_{nf}$  and the normal unloading capacity is  $\Delta\sigma_n$ ; the relationship is shown in Equation (1) and the values of all defined characteristic points are shown in Table 3.

$$\Delta\sigma_n = \sigma_{n0} - \sigma_{nf} \quad (1)$$

**Table 3.** All defined characteristic points.

$\theta$ (°)	$\sigma_{n0}$ (MPa)	$\tau_0$ (MPa)	$v$ (kN/s)	$D_{u1}$ (mm)	$D_{u2}$ (mm)	$D_{su}$ (mm)	$D_s$ (mm)	$D_{nu1}$ (mm)	$\sigma_{nf}$ (MPa)	$\Delta\sigma_n$ (MPa)
15	2.25	5.384	0.05	0.488	0.132	0.363	2.339	0.044	1.093	1.157
			0.10	0.420	0.108	0.115	0.458	0.020	1.148	1.102
			0.15	0.432	0.064	0.009	0.881	0.048	2.050	0.200
30	2.25	5.384	0.05	0.344	0.024	0.035	0.173	0.022	0.652	1.598
			0.10	0.532	0.056	0.028	0.213	0.052	0.889	1.361
			0.15	0.488	0.044	0.018	1.356	0.018	1.618	0.632
45	2.25	5.384	0.05	0.530	0.066	0.251	0.357	0.096	0.440	1.810
			0.10	0.348	0.078	0.209	0.441	0.014	0.606	1.644
			0.15	0.498	0.066	0.038	0.312	0.050	0.777	1.473

The evolution of characteristic displacements  $D_{u1}$ ,  $D_{u2}$ , and  $D_s$  are shown in Figure 7.

**Figure 7.** Evolution of  $D_{u1}$ ,  $D_{u2}$ , and  $D_s$ .

As shown in Figure 7, with an increase in  $\theta$ ,  $D_{u1}$  gradually increases, whereas  $D_{u2}$  and  $D_s$  gradually decrease. The increase in  $D_{u1}$  under each  $\theta$  is less than the height of a single asperity on the structural plane; specifically, the value of  $D_{u1}$  accounts for 59.70%, 31.81%, and 18.60% of the height of a single asperity under different  $\theta$ . Therefore, with an increase in  $\theta$ , the proportion of the increase in normal displacement gradually decreases. This shows that under the above-mentioned condition, the structural plane primarily undergoes elastic deformation. Therefore, the crack between the structural planes is compressed and the sawtooth tip is not damaged. In the second step,  $D_{u2}$  is greater than 0 mm, which indicates that the structural plane is further compressed. Meanwhile  $D_{u2} < D_{u1}$  indicates that the normal compression in the first step accounts for most of the compression. The structural plane is not damaged when the shear stress is applied to  $\tau_0$ ; therefore, it is no sliding with large displacement. With an increase in the  $\theta$ ,  $D_s$  gradually decreases, which corresponds to the length of a single asperity on the structural plane, i.e., 24.52%, 11.61%, and 7.4% of the length of a single asperity. Therefore, an increase in  $D_s$  corresponds to less than 1/4 of the length of a single asperity. Thus, with an increase in the  $\theta$ , the height of the corresponding single asperity increases, the “interlocking effect” of the upper and lower structural planes



is stronger, and it is more difficult to overcome the sliding of the asperity frictions; thus, the shear deformation gradually decreases.

The evolution of  $D_{su}$  is shown in Figure 8. Evidently, with an increase in  $v$ ,  $D_{su}$  gradually decreases. Therefore, the greater the value of  $v$ , the smaller would be the shear displacement before instability. Therefore, as  $v$  increases, the structural plane instability becomes more sudden, which is difficult to monitor. However, when  $v$  is small, the contingency of the structural plane instability is reduced; therefore, it has strong early warning and can be monitored.

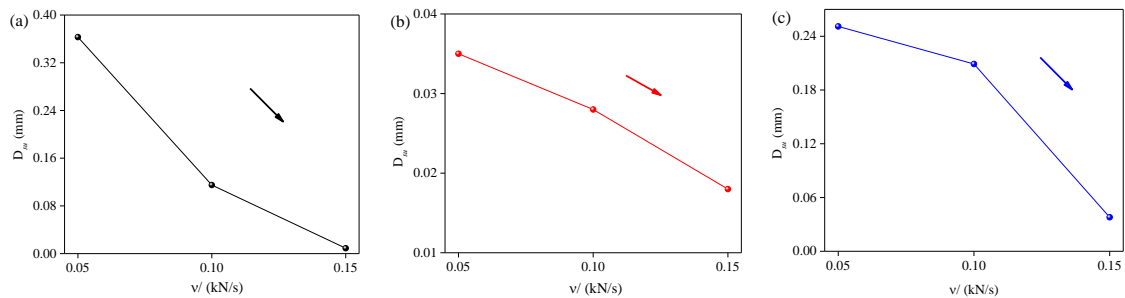


**Figure 8.** Evolution of  $D_{su}$ : (a)  $\theta = 15^\circ$ , (b)  $\theta = 30^\circ$ , (c)  $\theta = 45^\circ$ .

### 3.2. Failure Normal Stress

The evolutions of  $\sigma_{nf}$  and  $\Delta\sigma_n$  are shown in Figure 9. Evidently, with an increase in  $\theta$ ,  $\sigma_{nf}$  gradually decreases, which indicates that it is more difficult for the structural plane to become unstable and damaged in the process of unloading normal stress. With an increase in  $v$ ,  $\sigma_{nf}$  gradually increases, which indicates that the structural plane is more prone to instability. Therefore,  $\theta$  and  $v$  have the opposite effect on the instability of the structural plane. From Equation (1), it is evident that  $\sigma_{nf}$  and  $\Delta\sigma_n$  exhibit the opposite trend with changes in  $\theta$  and  $v$ . Correspondingly, with an increase in  $\theta$ ,  $\Delta\sigma_n$  gradually increases, but with an increase in  $v$ ,  $\Delta\sigma_n$  gradually decreases. It is also verified that  $\theta$  and  $v$  have the opposite effect on the stability of the structural plane. The action mechanism of  $\theta$  is primarily reflected in the “interlocking effect” of the upper and lower asperities on the structural plane. When  $\theta$  is small, the heights of the asperities on the corresponding structural plane are 0.67 mm; thus, it does not fit well. Moreover, the corresponding internal friction angle is small; the structural plane easily overcomes friction and slip failure. However, when  $\theta$  is large, the heights of the asperities increase, the “interlocking effect” between the asperities increases, the corresponding internal friction angle is larger, and the sliding failure of the structural plane is relatively difficult to achieve. Therefore,  $\Delta\sigma_n$  is an important safety factor that can be used to characterize the excavation stability; this is of great potential significance to the evaluation of the rock excavation.

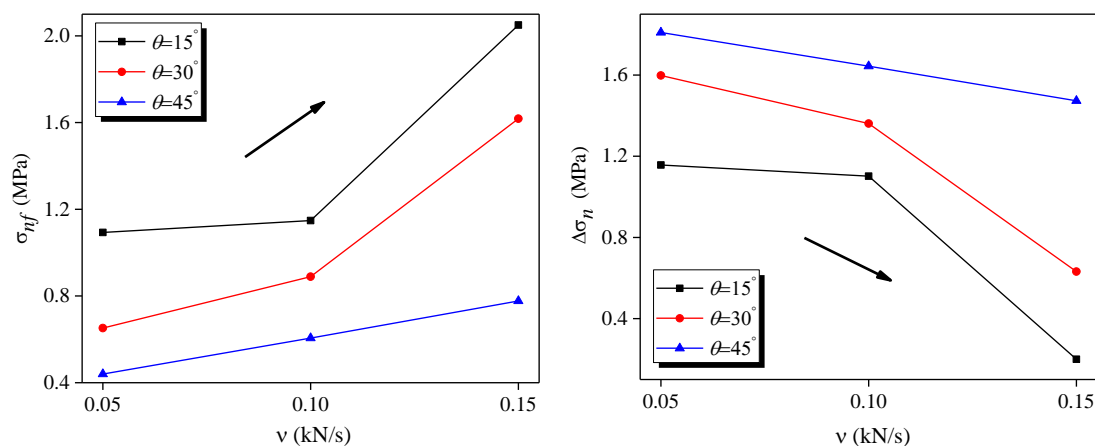


**Figure 9.** Evolutions of  $\sigma_{nf}$  and  $\Delta\sigma_n$ .

### 3.3. Energy Evolution Analysis

#### 3.3.1. Energy Calculation Method

In the compression shear test of a structural plane, the total work performed by external force is the sum of the work performed by normal force and shear force. The calculation method of work performed by external force is shown in Figure 10. Consequently, the energy can be calculated using the following formula:

$$U = U_n + U_s \quad (2)$$

$$U_n = \int_0^{D_n} F_n dD_n \quad (3)$$

$$U_s = \int_0^{D_n} F_n dD_n \quad (4)$$

where,  $U_n$  and  $U_s$  are the total work done by the normal force and shear force, respectively.

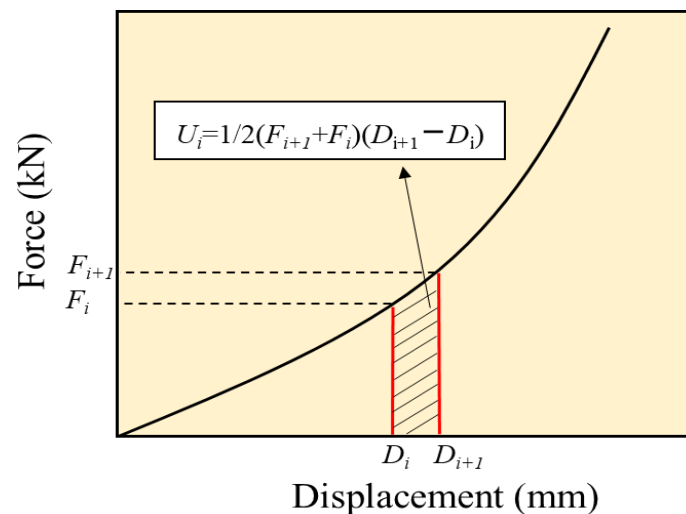


**Figure 10.** Calculate of work done by external force.

#### 3.3.2. Evolution of Energy

The energy evolution is shown in Figure 11. Evidently, in the first step, when the normal stress is applied, the structural plane is in the compression stage; the normal force performs positive work. The shear force is not applied;  $U_s = 0$  J, and  $U$  in this stage equals  $U_n$ . The evolution curve of  $U$  essentially coincides with the curve of  $U_n$ . In the second step, the normal stress is unchanged when the shear force is applied. Because the shear deformation direction is consistent with the direction of the shear force, the shear force performs positive work, and  $U_s$  exhibits a non-linear increasing trend. The shear force is applied while keeping the normal force unchanged; therefore, the structural plane is further compressed, and the normal force performs positive work. Owing to the small degree of compression, the increase in  $U_n$  is small.  $U_s$  and  $U$  increase nonlinearly and the growth rate between them is similar. In the third step, the direction of the normal displacement is opposite to that of the normal force; therefore, the normal force performs negative work and  $U_n$  decreases sharply. Moreover, the decreasing speed is equal to the normal stress. At this stage, the reduction in the normal force transforms the structural plane “from stability to instability”. The shear displacement has an increasing trend. As the  $U_s$  further increases, the increase in speed of  $U_s$  in the third step is considerably higher than that in the second step and there is a clear inflection point between the two stages.

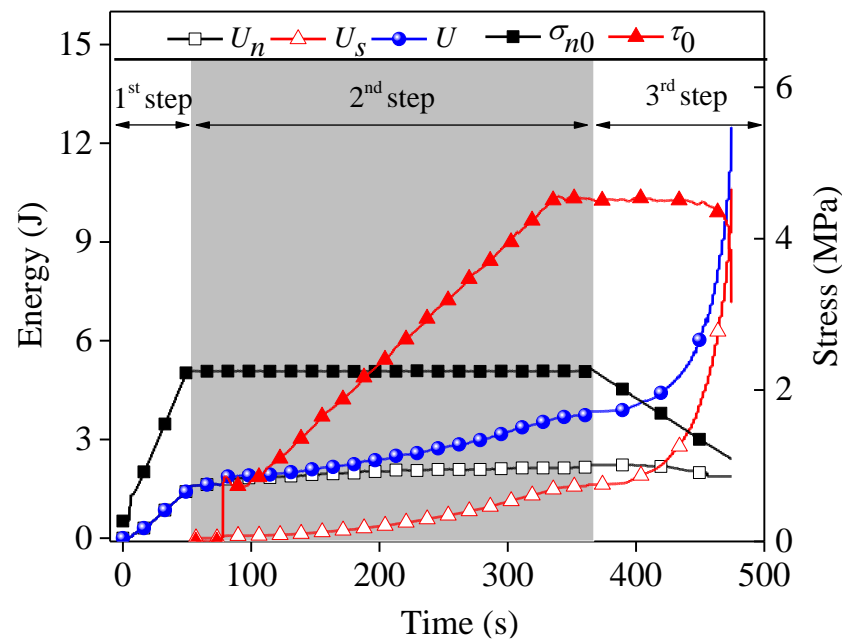


**Figure 11.** Energy time history evolution curve.

The values of  $U_n$ ,  $U_s$ , and  $U$  at the instability point are shown in Table 4.

**Table 4.** Values of  $U_n$ ,  $U_s$ , and  $U$ .

$\theta$ (°)	$\sigma_{n0}$ (MPa)	$\tau_0$ (MPa)	$v$ (kN/s)	$U_n$ (J)	$U_s$ (J)	$U$ (J)
15	2.25	5.384	0.05	1.876	3.613	5.489
			0.10	2.055	2.834	4.889
			0.15	2.605	2.490	5.095
30	2.25	5.384	0.05	0.535	4.098	1.633
			0.10	1.392	3.042	4.434
			0.15	1.497	2.966	4.463
45	2.25	5.384	0.05	1.565	4.576	6.141
			0.10	1.653	3.413	5.066
			0.15	1.727	3.217	4.944

The evolutions of  $U_n$  and  $U_s$  are shown in Figure 12. As shown in Figure 12a,  $U_n$  increases gradually with an increase in  $v$ . Therefore,  $U_n$  released under the same  $\theta$  decreases gradually; this also verifies that the structural plane is more prone to instability at a higher  $v$ . As observed in Figure 12b, at the unloading point,  $U_s$  gradually increases with an increase in  $\theta$ . However,  $U_s$  gradually decreases with an increase in  $v$ . Therefore, we can conclude that with an increase in  $v$ , the shear displacement generated when the structural plane is unstable is small; thus, the “impact tendency” is stronger and there is no clear transition period. Before reaching the instability point, the structural plane exhibits no obvious sliding and when it reaches the instability point, it exhibits “instantaneous” sliding. With an increase in  $\theta$ ,  $U_s$  at the unloading point gradually increases. When the structural plane is unstable, it is accompanied by the release of deformation energy stored between the structural planes. Therefore, with an increase in  $\theta$ , the structural plane instability occurs with a higher energy release.

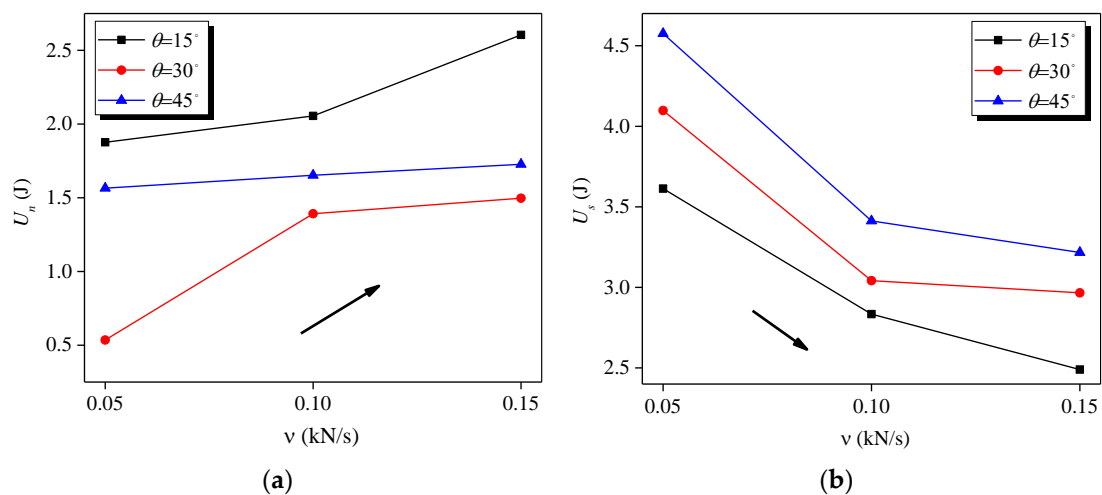


Figure 12. Energy evolution. (a)  $U_u$ ; (b)  $U_s$ .

The total energy difference  $\Delta U$  between the unloading and instability points is shown in Figure 13. Evidently,  $\Delta U$  gradually decreases with an increase in  $v$ . When  $v = 0.15$  kN/s,  $\Delta U$  decreases almost to 0 J; this shows that when the unloading starts to cause instability, the total energy contained in the structural plane is almost completely released, and the instability and failure degree of the rock mass increase gradually. With an increase in  $\theta$ ,  $\Delta U$  increases gradually, which indicates that the total energy loss decreases gradually in the unloading process. When  $\theta$  is small, the structural plane is prone to instability. With an increase in  $\theta$ , the total energy consumed in the process from unloading to instability is large; thus, instability in the structural plane becomes difficult. However, from the beginning of the unloading to the instability of the structural plane, the impact tendency during instability is lower, owing to the excessive total energy consumption. This indicates that  $\theta$  is inversely proportional to the impact tendency of the instability.

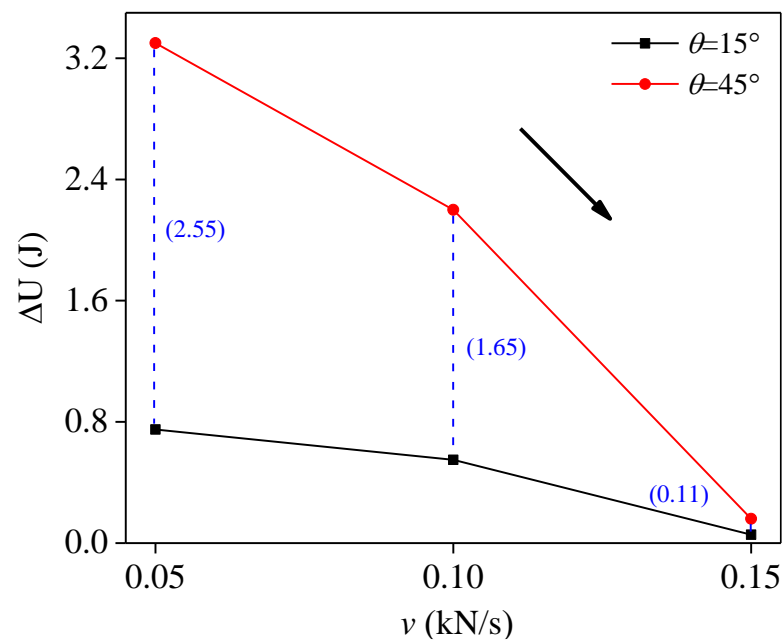
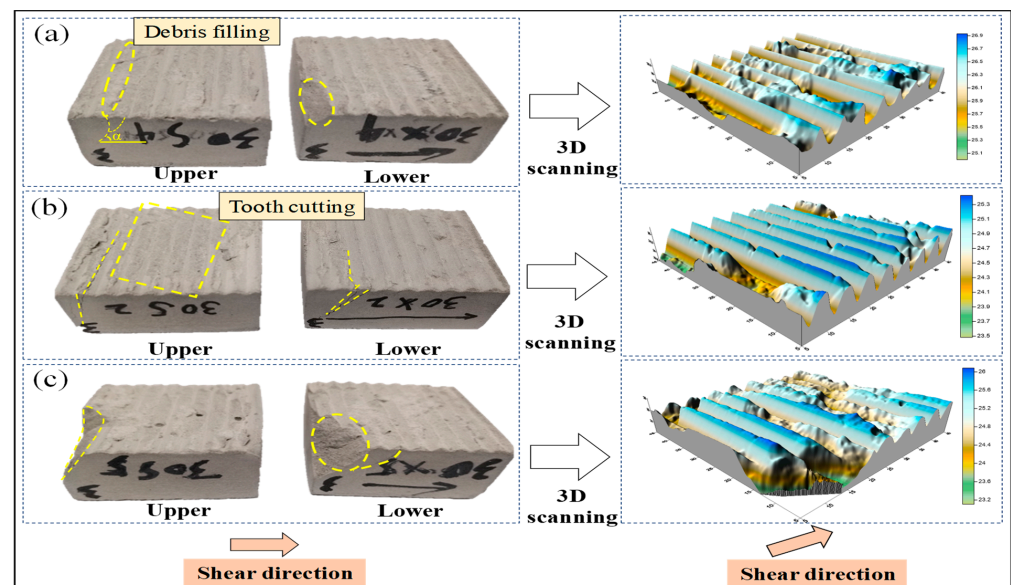


Figure 13. Total energy difference between unloading point and instability point.

### 3.4. Failure Pattern

Owing to length limitations,  $\theta = 30^\circ$  is considered as an example to analyze the failure mode of the structural plane, as shown in Figure 14.



**Figure 14.** Failure patterns of structure plane under  $\theta = 30^\circ$ : (a)  $v = 0.05$  kN/s, (b)  $v = 0.10$  kN/s, (c)  $v = 0.15$  kN/s.

The extent of damage can be directly observed from the visual diagram and 3D scanning diagram of the structural plane. We can directly see the damage degree of the structural plane under different  $v$ . When  $v = 0.05$  kN/s (Figure 14a), the wear degree of the upper and lower structural planes is low and only the half in front of the upper structure plane is filled with debris. Owing to stress concentration, some rock walls at the front of the lower structure plane are cut off in a small range. Tensile cracks are generated on the rock wall of the upper structural plane, the angle  $\alpha$  between the upper structural plane and the horizontal plane is an acute angle, and the wear degree of the asperities are lower. When  $v = 0.10$  kN/s (Figure 14b), the damage of the structural plane increases significantly and a tension crack is formed at the front end of the rock wall of the upper and lower structural planes. At this time, the crack is not limited to the rock wall and a through crack is also formed on the structural plane. The sawtooth cutting effect occurs in the middle of the upper structural plane. When  $v = 0.15$  kN/s (Figure 14c), the structural plane is most damaged. This is primarily reflected in the front end of the upper and lower structural planes, which is completely cut off, and tension cracks are formed on the rock wall of the lower structural plane. Similarly, this can be seen from the 3D morphology scanning.

The type and mechanism of rock burst can be predicted by the damage degree of the structural plane. The tensile cracks form on the surface wall of the structural plane and form an acute angle with the shear direction, that is, toward the free surface. Because the structural plane in engineering rock mass is not limited by the shear box, when the structural plane produces instantaneous failure, a large number of rock masses within the range from the tensile fracture surface to the free surface are washed away, thus forming large-scale explosion pits. With the increase in  $v$ , the damage degree of the structural plane increases; therefore, the grade of rock burst also increases gradually. It can be concluded that  $v$  is an important factor affecting the rock burst degree. Therefore, comprehensively understanding the geology and geomorphology and formulating perfect and accurate construction schedule are of great significance to the stability of engineering rock mass, which can ensure the safety of personnel and property to the greatest extent.

After 3D reconstruction, each structural plane is divided into five equal parts and four 2D profile lines are obtained, which is far in line with the three quantitative standards recommended by ISRM. The position of the profile line is at 10, 20, 30, and 40 mm in the Y direction and the sampling interval is 0.125 mm. The positive direction of X is the shear direction, as shown in Figure 15. According to the above definition, 2D section lines of the structural plane are obtained under different  $v$ , as shown in Figure 16.

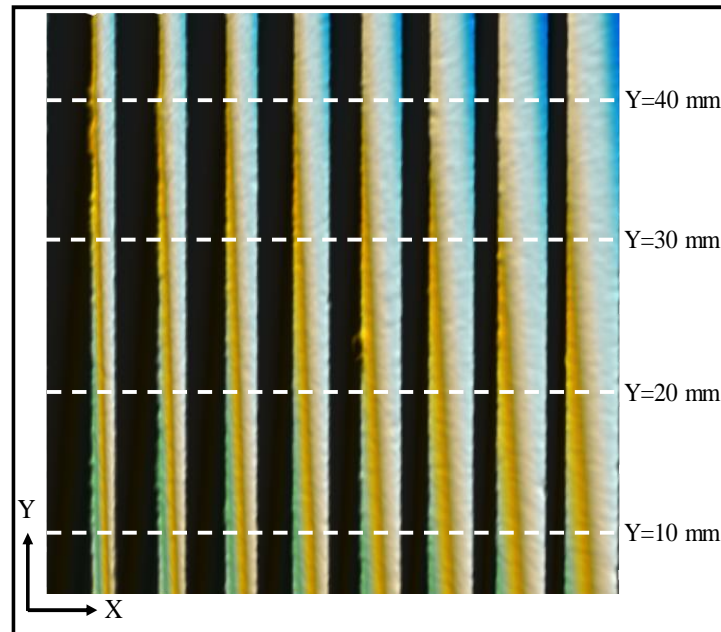


**Figure 15.** Schematic of 2D section line position of structural plane.

It can be seen from Figure 16 that the shape of the 2D section line of the structural plane changes after shearing. When  $v = 0.05$  kN/s, there are still a large number of undamaged regular sawteeth on the structural plane at different Y positions. When  $v = 0.10$  kN/s, most of the sawteeth on the structural plane are cut and they are filled between the structural planes, as can be seen from the increase in average height. When  $v = 0.15$  kN/s, the sawtooth on the same structural plane is cut off, however, compared with  $v = 0.10$  kN/s, there is no filler between the structural planes, indicating that the impact tendency of the structural plane is stronger. Therefore, with the increase in  $v$ , the damage degree of the structural plane increases and the “impact tendency” is stronger.

By analyzing the 2D section lines of the structural plane at different Y, the 2D morphological changes in the structural plane are obtained. Next, the damage degree of the structural plane is analyzed according to the evolution of the 3D morphological parameters. The 3D morphological parameters to be analyzed are defined as follows:

- (1) Average height  $z_3$ : the average height of each point on the structural plane;
- (2) Maximum height difference of surface  $S_h$ : vertical distance from the highest point to the lowest point of the structural plane;
- (3) Maximum peak height of surface  $S_p$ : the distance from the highest point of the structural plane to the datum plane;
- (4) Contour area ratio  $S_A$ : the ratio of the surface expanded area of the structural plane to the vertical projected area; the calculation equation is:

$$S_A = \frac{S_t}{S_n} \quad (5)$$

where  $S_t$  is the unfolded area of the surface and  $S_n$  is the area of the surface vertically projected to the bottom along the normal direction;

- (5) Volume  $V$ : the volume of the space enclosed by the structural plane and the bottom plane;
- (6) Surface area  $S_f$ : the expanded area of the surface of the structural plane.

The evolution of the 3D morphology parameters of the structural plane is shown in Figure 17. In the figure,  $v = 0$  kN/s represents the 3D morphology parameter value before shearing. It is evident from Figure 17 that the 3D morphological parameters after shearing are lower than those before shearing. Additionally, it decreases with the increase in  $v$ . It shows that the roughness of the structural plane decreases after shearing, therefore the damage degree gradually increases with the increase in  $v$ .

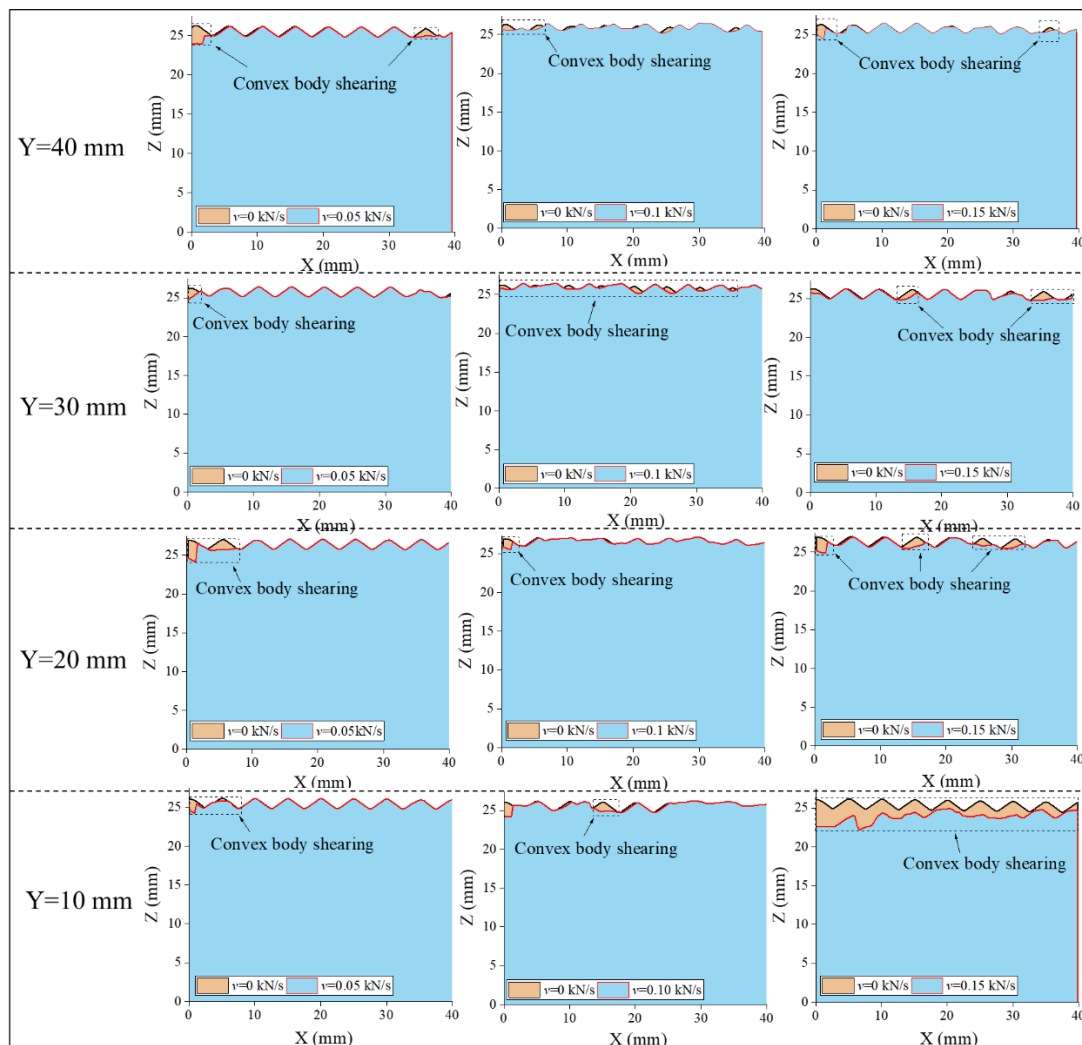


Figure 16. 2D section line of structural plane.

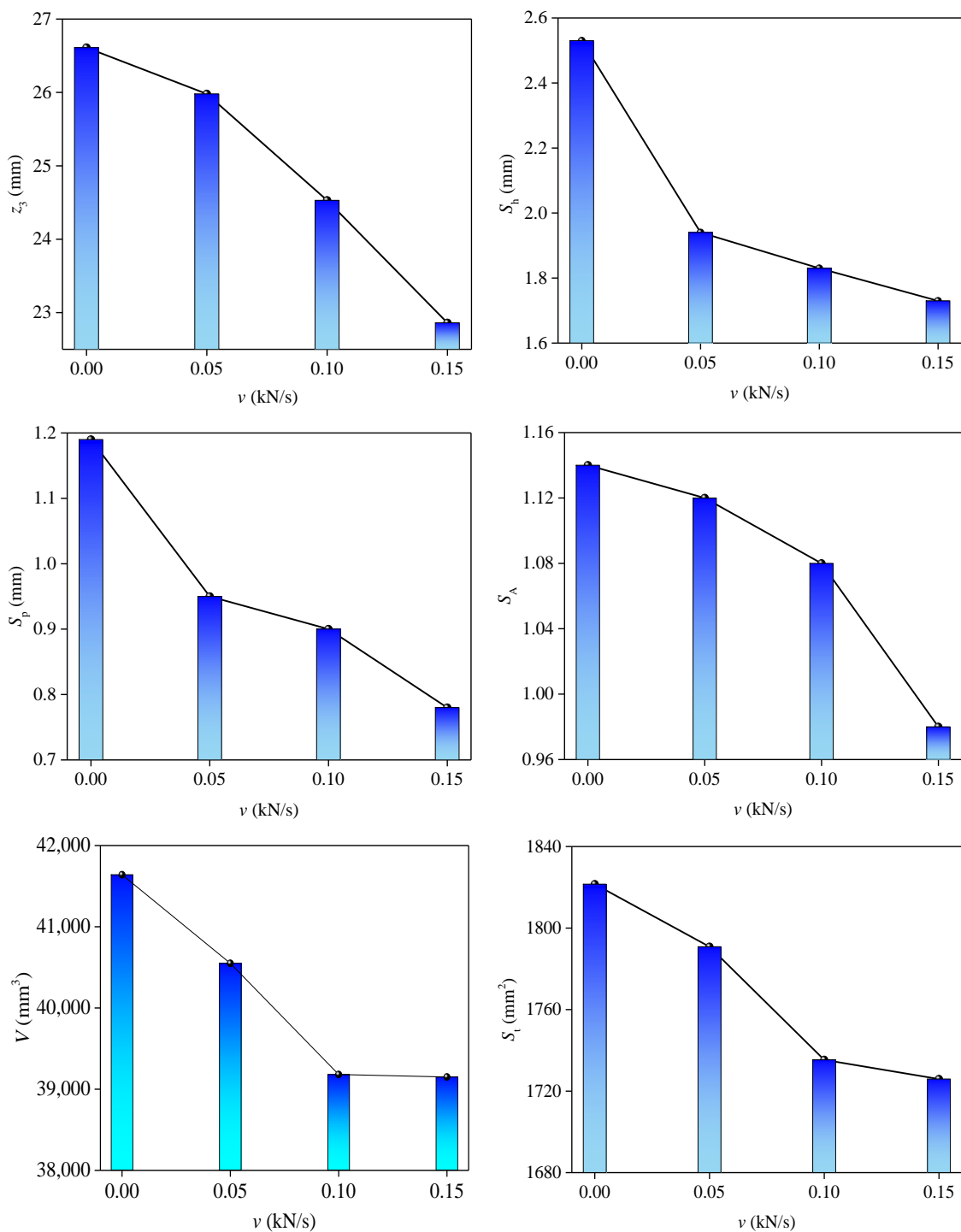


Figure 17. Evolution of 3D morphology parameters of structural plane.

#### 4. Discussion

##### 4.1. Gap Width Calculation Method

According to the research results obtained by the research team [46,47], the gap width during shearing can be characterized using point cloud data and normal deformation. The gap width refers to the spatial distribution of the spacing between the upper and lower structural planes, which is numerically equal to the difference between the z-axis coordinates of each point  $i$  ( $x,y$ ) on the upper and lower structural planes:

$$\Delta_i = z_{iu} - z_{id} \quad (6)$$



where,  $\Delta_i$  is the gap width at point  $i$ , and  $z_{iu}$  and  $z_{id}$  are the heights of the upper and lower structural planes at point  $i(x, y)$ , respectively.

The spatial position of each identification point on the upper and lower structural planes at different shear displacement is calculated through the point cloud data of the structural plane in Figure 14 and the shear displacement and normal displacement values of the structural plane at the starting point, unloading point, and instability point. Consequently, the distribution and evolution of the gap width of the structural plane in the shear process are analyzed. In the initial state (shear displacement  $u = 0$  mm), the 3D optical scanning technology can accurately obtain the space coordinate points  $i_{ou}(x, y, z)$  and  $i_{od}(x, y, z)$  of the upper and lower structural planes. When  $u = 0$  mm,  $z_{iou}$  and  $z_{iod}$  are  $z_{iu}$  and  $z_{id}$ , so  $z_{iou}$  and  $z_{iod}$  can be substituted into Equation (6) for direct calculation. For the gap width distribution with shear displacement,  $u \neq 0$  mm; its coordinates translate along the shear direction, therefore, it is necessary to calculate the coordinates of the upper and lower structural planes with any  $u$  through coordinate transformation. When the shear displacement is  $u$ , the gap width at each point on the structural plane can be deduced as follows:

$$\begin{cases} \Delta_i = z_{iou} - z_{iod}, u = 0 \text{ mm} \\ \Delta_i = z_{(i+u)ou} - z_{iod}, u \neq 0 \text{ mm} \end{cases} \quad (7)$$

where,  $z_{iou}$  is the height of the upper structural plane at point  $i$  in the initial state;  $z_{iod}$  is the height of the lower structural plane at point  $i$  in the initial state;  $z_{(i+u)ou}$  is the height of the upper structural plane at point  $(i + u)$  in the initial state; and  $\delta_n$  is the normal displacement when the shear displacement is  $u$ .

#### 4.2. Analysis of Impact Tendency of Structural Plane

As a result of the aforementioned analysis, the evolution of gap width with different  $\theta$  was obtained as shown in Figure 18.

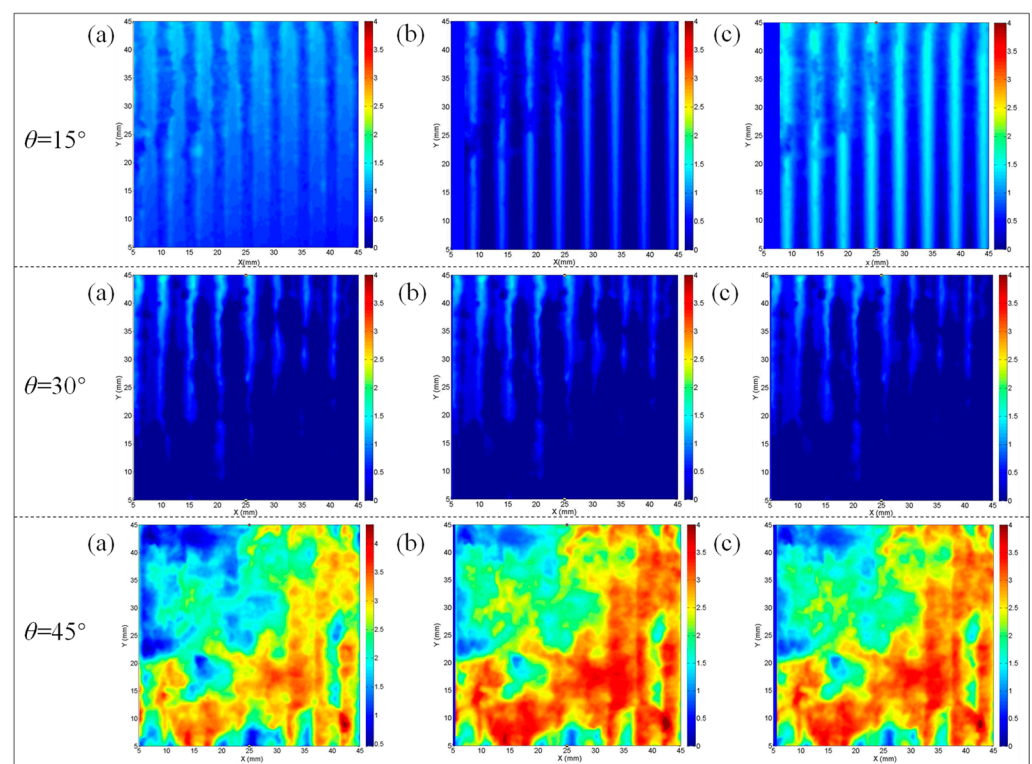


**Figure 18.** Evolution of gap width under different  $\theta$ . (a) Initial point; (b) unloading point; (c) instability point.

In Figure 18a–c represent the gap width corresponding to the structural plane at the initial point, unloading point, and instability point, respectively. Apparently, with the increase in the  $\theta$ , the gap width at the corresponding position increases gradually. At the same time, the change of the gap width gradually decreases, that is, the gap at the adjacent position basically does not change, indicating that the impact tendency of the structural plane instability is smaller.

The evolution of the gap width under different  $v$  is shown in Figure 19. Similarly, under each  $v$ , (a–c) represent the gap width at the initial point, unloading point, and instability point, respectively. Evidently, with the increase in  $v$ , the damage degree in the structural plane increases and the change of adjacent positions decreases, so the impact tendency is stronger.

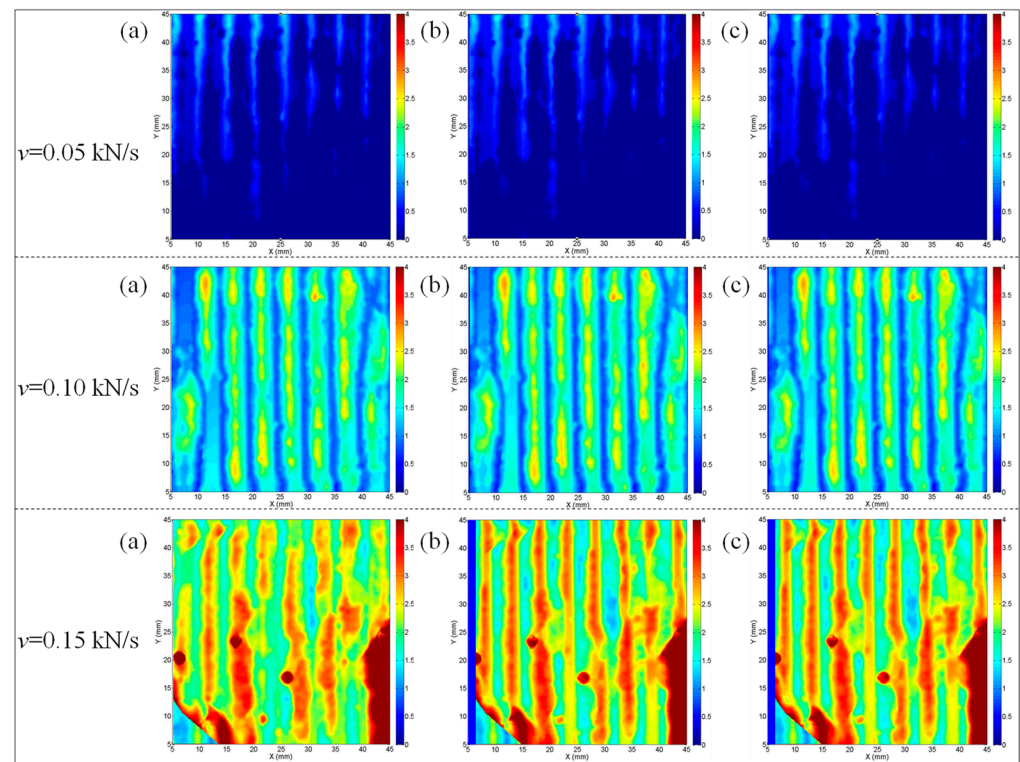


**Figure 19.** Evolution of structural plane gap width under different  $v$ . (a) Initial point; (b) unloading point; (c) instability point.

As the shear box is sealed, the structural plane cannot be taken out for 3D scanning in the three stages, so the 3D scanning map of each stage cannot be obtained in real time, which affects the accuracy of the gap width results. It is recommended that the shear box and the upper and lower structural planes be created with resin materials at the same time, so that the structural plane morphology can be scanned in real time and the 3D point cloud data obtained are more accurate, meaning the accuracy of the test results can be further improved. In future research, work should focus on the establishment of the structural plane visualization system.

## 5. Conclusions

This study analyzes the influence of  $\theta$  and  $v$  on the evolution laws of characteristic displacement, failure strength, 3D morphology parameters, and energy of the structural plane through the unloading normal stress test. The main conclusions of the study are as follows:

- (1) In the first step, the normal displacement increases nonlinearly and the increase rate decreases gradually. In the second step, the shear displacement increases linearly

and the increase rate is 0.001 mm/s. In the third step, the normal displacement decreases nonlinearly, the reduction rate increases gradually and the shear displacement increases nonlinearly until the instability of the structural plane occurs. With an increase in  $\theta$ , the  $D_{u1}$  gradually increases, however,  $D_{u2}$  and  $D_s$  gradually decrease. The increase in  $D_{u1}$  is less than the height of a single asperity on the structural plane.  $D_{su}$  and  $\sigma_{nf}$  decrease gradually with an increase in the  $v$ .

- (2) With an increase in  $v$ , the  $U_n$  increases gradually and  $U_n$  released under the same  $\theta$  decreases gradually. At the unloading point,  $U_s$  increases gradually with an increase in  $\theta$ . However,  $U_s$  decreases gradually with an increase in  $v$ . With an increase in  $\theta$ ,  $U_s$  at the unloading point increases gradually.
- (3) The tension crack that forms on the wall of the structural plane is at an acute angle with the shear direction. By analyzing the evolution of the 2D section line and 3D morphology parameters of the structural plane, it is obtained that the damage degree of the structural plane increases with the increase in  $v$ . Meanwhile, an analysis of the evolution of the gap width of the structural plane, with the decrease in the  $\theta$  or the increase in  $v$ , demonstrates that the ability of instability failure of the structural plane increases while the impact tendency of the structural plane, however, decreases.

**Author Contributions:** J.X.: contributed to experimental design. F.J. and S.P.: conducted the experiment. S.P. and F.J.: analyzed the data and wrote the main manuscript text. All authors reviewed the manuscript. All authors have read and agreed to the published version of the manuscript.

**Funding:** This work was supported and financed by the National Natural Science Foundation of China [grant No. 51874055; 51974041].

**Institutional Review Board Statement:** Not applicable.

**Informed Consent Statement:** Not applicable.

**Data Availability Statement:** No data was used for the research described in the article.

**Conflicts of Interest:** The authors declare that they have no known competing financial interests or personal relationships that could have appeared to influence the work reported in this paper.

## References

1. Cai, M.; Kaiser, P. In-situ rock spalling strength near excavation boundaries. *Rock Mech. Rock Eng.* **2014**, *47*, 659–675. [[CrossRef](#)]
2. Feng, F.; Chen, S.; Li, D.; Hu, S.; Huang, W.; Li, B. Analysis of fractures of a hard rock specimen via unloading of central hole with different sectional shapes. *Energy Sci. Eng.* **2019**, *7*, 2265–2286. [[CrossRef](#)]
3. Zhao, Z.; Tan, Y.; Chen, S.; Ma, Q.; Gao, X. Theoretical analyses of stress field in surrounding rocks of weakly consolidated tunnel in a high-humidity deep environment. *Int. J. Rock Mech. Min. Sci.* **2019**, *122*, 104064. [[CrossRef](#)]
4. Yang, Z.; Chiang, D. An experimental study on the progressive shear behavior of rock joints with tooth-shaped asperities. *Int. J. Rock Mech. Min. Sci.* **2000**, *37*, 1247–1259. [[CrossRef](#)]
5. Li, H.; Liu, M.; Xing, W.; Shao, S.; Zhou, J. Failure mechanisms and evolution assessment of the excavation damaged zones in a large-scale and deeply buried underground powerhouse. *Rock Mech. Rock Eng.* **2017**, *50*, 1883–1900. [[CrossRef](#)]
6. Cai, M. Influence of intermediate principal stress on rock fracturing and strength near excavation boundaries-Insight from numerical modeling. *Int. J. Rock Mech. Min. Sci.* **2008**, *45*, 763–772. [[CrossRef](#)]
7. Zhang, Z.; Deng, M.; Bai, J.; Yu, X.; Wu, Q.; Jiang, L. Strain energy evolution and conversion under triaxial unloading confining pressure tests due to gob-side entry retained. *Int. J. Rock Mech. Min. Sci.* **2020**, *126*, 104184. [[CrossRef](#)]
8. Si, X.; Gong, F. Strength-weakening effect and shear-tension failure mode transformation mechanism of rockburst for fine-grained granite under triaxial. *Int. J. Rock Mech. Min. Sci.* **2020**, *131*, 104347. [[CrossRef](#)]
9. Li, D.; Sun, Z.; Xie, T.; Li, X.; Ranjith, P. Energy evolution characteristics of hard rock during triaxial failure with different loading and unloading paths. *Eng. Geol.* **2017**, *228*, 270–281. [[CrossRef](#)]
10. Wang, X.; Cui, J.; Zhu, C.; Wu, Y.; Wang, X. Experimental study of the mechanical behavior of calcareous sand under repeated loading-unloading. *Bull. Eng. Geol. Environ.* **2021**, *80*, 3097–3113. [[CrossRef](#)]
11. Liang, Y.; Li, Q.; Gu, Y.; Zou, Q. Mechanical and acoustic emission characteristics of rock: Effect of loading and unloading confining pressure at the postpeak stage. *J. Nat. Gas Sci. Eng.* **2017**, *44*, 54–64. [[CrossRef](#)]
12. Wang, K.; Zhang, X.; Du, F.; Xin, C.; Wang, L. Coal damage and permeability characteristics under accelerated unloading confining pressure. *Geotech. Geol. Eng.* **2020**, *38*, 561–572. [[CrossRef](#)]

13. Huang, H.; Huang, M.; Ding, J. Calculation of tangent modulus of soils under different stress paths. *Math. Probl. Eng.* **2018**, *5*, 1916761. [[CrossRef](#)]
14. Shi, C.; Yang, J.; Chu, W.; Tang, H.; Zhang, Y. Macro-and micromechanical behaviors and energy variation of sandstone under different unloading stress paths with DEM. *Int. J. Geomech.* **2021**, *21*, 04021127. [[CrossRef](#)]
15. Zhang, Y.; Yang, Y.; Ma, D. Mechanical characteristics of coal samples under triaxial unloading pressure with different test paths. *Shock Vib.* **2020**, *1*, 8870821. [[CrossRef](#)]
16. Zhang, J.; Song, Z.; Wang, S. Experimental investigation on permeability and energy evolution characteristics of deep sandstone along a three-stage loading path. *Bull. Eng. Geol. Environ.* **2021**, *80*, 1571–1584. [[CrossRef](#)]
17. Xie, H.; He, C. Study of the unloading characteristics of a rock mass using the triaxial test and damage mechanics. *Int. J. Rock Mech. Min. Sci.* **2004**, *41*, 366. [[CrossRef](#)]
18. Yang, Y.; Jiang, C.; Guo, X.; Peng, S.; Zhao, J.; Yan, F. Experimental investigation on the permeability and damage characteristics of raw coal under tiered cyclic unloading and loading confining pressure. *Powder Technol.* **2021**, *389*, 416–429. [[CrossRef](#)]
19. Ren, J.; Chen, X.; Chen, X.; Yun, M.; Liu, T. Effect of porewater pressure on the mechanical properties of red sandstone with different unloading rates. *Q. J. Eng. Geol. Hydrogeol.* **2021**, *54*, 1–16. [[CrossRef](#)]
20. Li, D.; Sun, Z.; Zhu, Q.; Peng, K. Triaxial loading and unloading tests on dry and saturated sandstone specimens. *Appl. Sci.* **2019**, *9*, 1689. [[CrossRef](#)]
21. Peng, K.; Zhang, J.; Zou, Q.; Song, X. Deformation characteristics of granites at different unloading rates after high-temperature treatment. *Environ. Earth Sci.* **2020**, *79*, 343. [[CrossRef](#)]
22. Wang, J.; Fu, J.; Song, W. Mechanical properties and microstructure of layered cemented paste backfill under triaxial cyclic loading and unloading. *Constr. Build. Mater.* **2020**, *257*, 119540. [[CrossRef](#)]
23. Huang, D.; Li, Y. Conversion of strain energy in triaxial unloading tests on marble. *Int. J. Rock Mech. Min. Sci.* **2014**, *66*, 160–168. [[CrossRef](#)]
24. Liu, S.; Zhu, Q.; Shao, J. Deformation and mechanical properties of rock: Effect of hydromechanical coupling under unloading conditions. *Bull. Eng. Geol. Environ.* **2020**, *79*, 5517–5534. [[CrossRef](#)]
25. Xu, J.; Li, H.; Meng, Q.; Xu, W.; He, M.; Yang, J. A study on triaxial unloading test of columnar-jointed-rock-mass-like material with wave velocity analysis. *Adv. Civ. Eng.* **2020**, *10*, 6693544. [[CrossRef](#)]
26. Wang, J.; Liu, M.; Jian, F.; Chai, H. Mechanical behaviors of a sandstone and mudstone under loading and unloading conditions. *Environ. Earth Sci.* **2019**, *78*, 30. [[CrossRef](#)]
27. Wang, Y.; Feng, W.; Hu, R.; Li, C. Fracture evolution and energy characteristics during marble failure under triaxial fatigue cyclic and confining pressure unloading (FC-CPU) conditions. *Rock Mech. Rock Eng.* **2021**, *54*, 799–818. [[CrossRef](#)]
28. Dai, B.; Zhao, G.; Konietzky, H.; Wasantha, P. Experimental and numerical study on the damage evolution behaviour of granitic rock during loading and unloading. *KSCE J. Civ. Eng.* **2018**, *22*, 3278–3291. [[CrossRef](#)]
29. Yang, S.; Ju, Y.; Gao, F.; Gui, Y. Strength, Deformability and X-ray Micro-CT observations of deeply buried marble under different confining pressures. *Rock Mech. Rock Eng.* **2016**, *49*, 4227–4244. [[CrossRef](#)]
30. Zhao, Y.; Bi, J.; Wang, C.; Liu, P. Effect of unloading rate on the mechanical behavior and fracture characteristics of sandstones under complex triaxial stress conditions. *Rock Mech. Rock Eng.* **2021**, *54*, 4851–4866. [[CrossRef](#)]
31. Chen, Y.; Zuo, J.; Li, Z.; Dou, R. Experimental investigation on the crack propagation behaviors of sandstone under different loading and unloading conditions. *Int. J. Rock Mech. Min. Sci.* **2020**, *130*, 104310. [[CrossRef](#)]
32. Chen, Y.; Guo, W.; Zuo, J.; Shuai, H.; Dou, R. Effect of triaxial loading and unloading on crack propagation and damage behaviors of sandstone: An experimental study. *Rock Mech. Rock Eng.* **2021**, *54*, 6077–6090. [[CrossRef](#)]
33. Ding, Q.; Ju, F.; Mao, X.; Ma, D.; Yu, B.; Song, S. Experimental investigation of the mechanical behavior in unloading conditions of sandstone after high-temperature treatment. *Rock Mech. Rock Eng.* **2016**, *49*, 2641–2653. [[CrossRef](#)]
34. Zhao, J.; Zhang, T. Experimental study on mechanical properties of deep buried granite under different confining pressures. *Adv. Civ. Eng.* **2020**, *5*, 6640497. [[CrossRef](#)]
35. Peng, R.; Ju, Y.; Wang, J.; Xie, H.; Gao, F.; Mao, L. Energy dissipation and release during coal failure under conventional triaxial compression. *Rock Mech. Rock Eng.* **2015**, *48*, 509–526. [[CrossRef](#)]
36. Meng, Q.; Liu, J.; Huang, B.; Pu, H.; Wu, J.; Zhang, Z. Effects of confining pressure and temperature on the energy evolution of rocks under triaxial cyclic loading and unloading conditions. *Rock Mech. Rock Eng.* **2022**, *55*, 773–798. [[CrossRef](#)]
37. Chang, Y.; Chen, Z.; Ren, F.; Chang, L. Strain energy dissipation and damage evolution of frozen migmatite under triaxial unloading. *Geotech. Geol. Eng.* **2019**, *37*, 3183–3192. [[CrossRef](#)]
38. Duan, S.; Jiang, Q.; Xu, D.; Liu, G. Experimental study of mechanical behavior of interlayer staggered zone under cyclic loading and unloading condition. *Int. J. Geomech.* **2020**, *20*, 04019187. [[CrossRef](#)]
39. Zhang, Y.; Wang, L.; Li, H.; Zhang, Y.; Fu, G. Experimental study of the permeability of fractured sandstone under complex stress paths. *Energy Sci. Eng.* **2020**, *8*, 3217–3227. [[CrossRef](#)]
40. Wang, C.; Liu, J.; Chen, L.; Liu, J.; Wang, L. Mechanical behaviour and damage evolution of Beishan granite considering the transient and time-dependent effects of excavation unloading. *Eur. J. Environ. Civ. Eng.* **2020**, *1*, 3187–3203. [[CrossRef](#)]
41. Zhu, T.; Huang, D. Experimental investigation of the shear mechanical behavior of sandstone under unloading normal stress. *Int. J. Rock Mech. Min. Sci.* **2019**, *114*, 186–194. [[CrossRef](#)]

42. Beer, A.; Stead, D.; Coggan, J. Estimation of the joint roughness coefficient (JRC) by visual. *Rock Mech. Rock Eng.* **2002**, *35*, 65–74. [[CrossRef](#)]
43. Hong, E.; Lee, J.; Lee, I. Underestimation of roughness in rough rock joints. *Int. J. Numer. Anal. Met.* **2008**, *32*, 1385–1403. [[CrossRef](#)]
44. Yang, J.; Yang, X.; Zhou, J.; Liu, Y.; Dong, B.; Li, H. Comparative study of the excavation damage and rockburst of the deeply buried Jinping II diversion tunnels using a TBM and the drilling-blasting method. *Adv. Civ. Eng.* **2020**, *2*, 8876214. [[CrossRef](#)]
45. Xu, J.; Liu, Y.; Yin, G.; Li, B.; Peng, S.; Ye, G. Development of shear-flow coupling test device for coal rock. *Chin. J. Rock Mech. Eng.* **2015**, *34* (Suppl. S1), 2987–2995. [[CrossRef](#)]
46. Xu, J.; Lei, J.; Liu, Y.; Wu, J. Experimental study on shear behavior of joints filled with different materials. *Rock Soil Mech.* **2018**, *40*, 4129–4137. [[CrossRef](#)]
47. Xu, J.; Wu, J.; Liu, Y.; Lei, J. Experimental study of shear-seepage coupling properties of rock mass under different filling degrees. *Rock Soil Mech.* **2019**, *40*, 3416–3434. [[CrossRef](#)]